metals

MDPI

Article

Comparison of Nitriding Behavior for Austenitic Stainless Steel 316Ti and Super Austenitic Stainless Steel 904L

Stephan Mändl * and Darina Manova

Leibniz Institute of Surface Engineering (IOM), Permoserstr. 15, 04318 Leipzig, Germany; darina.manova@iom-leipzig.de

* Correspondence: stephan.maendl@iom-leipzig.de

Abstract: In situ X-ray diffraction (XRD) was used to compare nitrogen low-energy ion implantation (LEII) into austenitic stainless steel 316Ti and super austenitic stainless steel 904L. While the diffusion and layer growth were very similar, as derived from the decreasing intensity of the substrate reflection, strong variations in the observed lattice expansion—as a function of orientation, the steel alloy, and nitriding temperature—were observed. Nevertheless, a similar resulting nitrogen content was measured using time-of-flight secondary ion mass spectrometry (ToF-SIMS). Furthermore, for some conditions, the formation of a double layer with two distinct lattice expansions was observed, especially for steel 904L. Regarding the stability of expanded austenite, 316Ti had already decayed in CrN during nitriding at 500 °C, while no such effect was observed for 904L. Thus, the alloy composition has a strong influence only on the lattice expansion and the stability of expanded austenite—but not the diffusion and nitrogen content.

Keywords: expanded austenite; austenitic stainless steel; nitriding; in situ XRD

1. Introduction

Austenitic stainless steel is a rather soft material and is prone to high wear rates. Thus, the nitriding of austenitic stainless steel with the aim of increasing its tribological properties has been developed [1–3]. Here, nitrogen insertion in the temperature range between 300 and 450 °C leads to a super-saturated phase with nitrogen still in solid solution [4–9]. This so-called expanded austenite is a metastable phase which can accommodate nitrogen up to 38 at.%, resulting in anisotropic lattice expansion up to 12% [10]. However, it starts to decay into CrN/Cr_2N and a nitrogen-free Fe-Ni phase at around 450 °C [11].

Nevertheless, most of the existing work describes the behavior of the common alloys, such as 304 and 316L. Here, the fcc structure is stabilized at room temperature by adding just enough austenite stabilizing elements, such as Ni and Mn, while maintaining a high Cr content to allow passivation of the surface. For alloys with even higher Ni contents with improved and better corrosion resistance, which are commonly classified as Ni-base alloys, a similar formation of expanded austenite is observed [6]. In between the austenitic stainless steel and Ni-base alloys, there reside super austenitic stainless steels; they are considered to be steels with a Pitting Resistance Equivalent Number (PREN) greater than 40. Thus, much higher additions of Ni and Mo are necessary, combined with a lower Fe content, to obtain an even better corrosion resistance than that of austenitic stainless steel.

While there is a huge amount of literature on the nitriding process, with more than a dozen reviews summarizing the results for austenitic stainless steel [1,12–15], there is almost no information on the phase formation in super austenitic stainless steel. The nitriding of steel UNS S31254 between 400 and 500 °C resulted in expanded austenite with a lattice expansion of 5–10% [16]. At a treatment time of 5 h, the layer thickness after nitriding increased from 5 to 20 µm, with nitrocarburizing producing thicker layers [17]. At the same time, CrN precipitates have been identified with TEM even at 400 °C. Using the same steel alloy, nitriding at lower temperatures between 300 and 400 °C resulted in an

check for updates

Citation: Mändl, S.; Manova, D. Comparison of Nitriding Behavior for Austenitic Stainless Steel 316Ti and Super Austenitic Stainless Steel 904L. *Metals* **2024**, *14*, 659. https://doi.org/10.3390/met14060659

Academic Editor: Francesca Borgioli

Received: 25 April 2024
Revised: 29 May 2024
Accepted: 29 May 2024
Published: 1 June 2024

Copyright: © 2024 by the authors. Licensee MDPI, Basel, Switzerland. This article is an open access article distributed under the terms and conditions of the Creative Commons Attribution (CC BY) license (https://creativecommons.org/licenses/by/4.0/).

expanded phase [18]. However, at 400 °C, dispersed nitrides in a superficial region of about 400 nm have been observed using glancing angle XRD. Thus, it appears that the higher Ni content in super austenitic stainless steel may have some influence on the stability of the expanded phase, while no direct comparison of the diffusion and the actual nitrogen near the surface is possible from the literature data.

Hence, this manuscript compares the nitriding behavior and the stability of expanded austenite for AISI 316Ti and 904L using in situ X-ray diffraction during nitriding as well as during depth profiling by sputter etching. Thus, direct access to the diffusion, phase formation, and phase stability was possible without manufacturing a large set of samples. Furthermore, this assures that the time series is actually produced under identical conditions.

2. Materials and Methods

Two different stainless steels, the austenitic AISI 316Ti (X6CrNiMoTi17-12-2, equivalent to DIN 1.4571, according to DIN/EN (in wt.%) C $\leq$ 0.08, Cr 16.5–18.5, Ni 10.5–13.5, Mo 2.0–2.5, Ti 5 $\times$ C $\leq$ 0.70) and the super austenitic AISI 904L (X1NiCrMoCu25.20.5, equivalent to DIN 1.4539, according to DIN/EN (in wt.%) C $\leq$ 0.02, Cr 19.0–21.0, Ni 24.0–26.0, Mo 4.0–5.0, Cu 1.2–2.0) were used. Rods with 15 mm and 20 mm diameters, for 316Ti and 904L, respectively, furnished coupons with 2.5 mm thickness, which were ground and polished up to a mirror finish.

The experiments are a combination of low-energy ion implantation (LEII) and in situ XRD measurements in a vacuum system consisting of two chambers, an ion source chamber and an XRD chamber, with separated pumping systems for independent control of the vacuum conditions. Both chambers are connected by a gate valve. The XRD chamber contains a diffractometer in Bragg–Brentano geometry with an external sample heating system. Thus, it is possible to make an adjustment of ion current density independently of the process temperature. The sample temperature is measured closely to the sample surface during the whole experiment and can be kept constant via a fast control loop. More details on the experimental equipment can be found in [19]. At the same time, the narrow XRD substrate peaks for stainless steel can be used for a temperature control independently of the thermocouple with a resolution of better than 5 K.

An ion beam with an energy of up to 2 keV was produced by a broad beam Kaufman-type source [20,21]. It is movable inside the ion source chamber, allowing an in situ adjustment of the beam with respect to the sample holder in the XRD chamber. Before and after every experiment, the ion current density is measured using a Faraday cup, with the identical size and shape as the sample holder, placed on the position of the sample holder. The measurements confirmed the high stability of the ion source [19]. The acquisition time for one diffractogram encompassing a 2θ range from 35 to 54 deg is slightly less than 2 min as a position-sensitive linear X-ray detector is used. The wavelength of 0.15418 nm corresponds to Cu K_α radiation.

Depending on the ion species, nitriding and sputter etching can be performed. Nitrogen ions are formed and accelerated for nitriding, whereas noble gas ions, e.g., Ar, are employed for the sputter etching process. In the former case, the time-resolved X-ray data are indicative of the phase changes occurring during nitriding, averaged across the whole information depth. For austenitic stainless steel, this corresponds to a layer thickness of around 2.5 µm for the current angular range [22]. In the latter case, depth-resolved information on the phase formation can be obtained during sputter etching where no changes within the samples are supposed to occur (neither diffusion nor phase transformations). Hence, this allows us to convert the time series of the acquired X-ray diffractograms into a depth series with a depth resolution of 50 nm or better [23].

The studied samples were nitrided with 0.8 keV nitrogen ions. The temperature during the nitriding experiments was between 350 and 500 °C, with the samples being heated to this temperature before the process was begun. The ion current density was fixed at 180 µA/cm^2. The nitriding time varied between 90 and 180 min. For the sputter etching experiments, 0.9 keV argon ions were used. Here, the process temperature was maintained

at 180 °C; this elevated temperature was necessary to avoid the artificial peak shifts caused by a slow but noticeable heating of the sample during the whole experiment. However, no diffusion or phase transition processes were observed at this temperature, in agreement with the diffusion rates calculated from the activation energies reported in the literature [24]. Using the temporal evolution of the substrate X-ray reflections, the (orientation-dependent) sputter rate can be directly determined [23]. This calculation also serves as an independent check on the stability of the ion current.

ToF-SIMS measurements (IONTOF SIMS V, Münster, Germany) of the samples were carried out with 15 keV $^{69}Ga^+$ ions for the analysis and 2 keV O_2^+ ions for sputter profiling to obtain the nitrogen depth distribution. The scan areas were chosen to be 100 × 100 µm^2 and 300 × 300 µm^2, respectively, to avoid crater edge effects of the analysis beam. The ion beam current for analysis was about 2 pA, while the ion beam current for sputtering was around 700 nA, resulting in a surface removal rate of about 0.7–0.9 nm/s for the selected scan size. The thickness of the nitrided layers was determined from the respective crater depth, assuming a constant sputter rate within the implanted layer.

For the calibration of the count rate in SIMS, selected samples were additionally measured using GDOES by an external company (TAZ GmbH, Aichach, Germany accreditation according to [25]—a Europewide quality standard for analytical testing laboratories) with the established procedures used for nitrided steels; the following elements were measured: C, N, O, Fe, Cr, Ni, Mo, and S. Here, a typical circular crater size with a 2.5 mm diameter was formed.

Additionally, ex situ XRD measurements were conducted at room temperature after the end of the experiments using another XRD set-up (Rigaku SmartLab multi-purpose diffractometer system, Tokyo, Japan). The system is equipped with a 9 kW rotating Cu anode X-ray source, a primary Johansson Ge(111) Kα_1 monochromator (wavelength Cu Kα_1: 0.15406 nm), a 5-axis-goniometer, and a solid state area detector (HyPix-3000, Rigaku, Tokyo, Japan) with 0D, 1D, and 2D detection modes. The samples were measured in parallel beam geometry performing a continuous/accumulating 1D scan over the 2θ range of interest. The XRD measurements were recorded and evaluated using the Rigaku SmartLab Studio II software package.

3. Results

As the in situ measurements yield a plethora of information, several different aspects of the nitriding process can be investigated (as a function of time or a function of depth), using very few samples; furthermore, the introduction of inevitable errors can be avoided by using ex situ measurements for a larger number of samples within a time series. In the following subsections, (i) diffusion, (ii) lattice expansion, and (iii) peak splitting, as well as (iv) the stability of the expanded phase, are investigated in detail.

3.1. Diffusion

Figure 1a,b present the nitrogen depth profiles for both steel grades—904L and 316Ti—as a function of temperature, together with a calibration curve from GDOES as an insert. While the treatment time varies for the 904L samples by up to a factor of two between 90 and 186 min, the time is always 90 min for 316Ti. Nevertheless, some general tendencies can be extracted from the data. At 350 °C, a slower diffusion is observed for 904L, while similar diffusivities were encountered for the higher temperatures. The surface nitrogen content appears to have a maximum near 400 °C for both alloys, where up to 40 at.% was measured. The rather high nitrogen flux aggregates near the surface at this temperature as the diffusion is not fast enough to transport the nitrogen into deeper regions. As shown in panel Figure 1c, there is a very good correlation between the strong decrease in the nitrogen content and the region near the surface, where a different etching contrast is observed. As the original grains are still visible, it can be assumed that no CrN precipitates are formed.

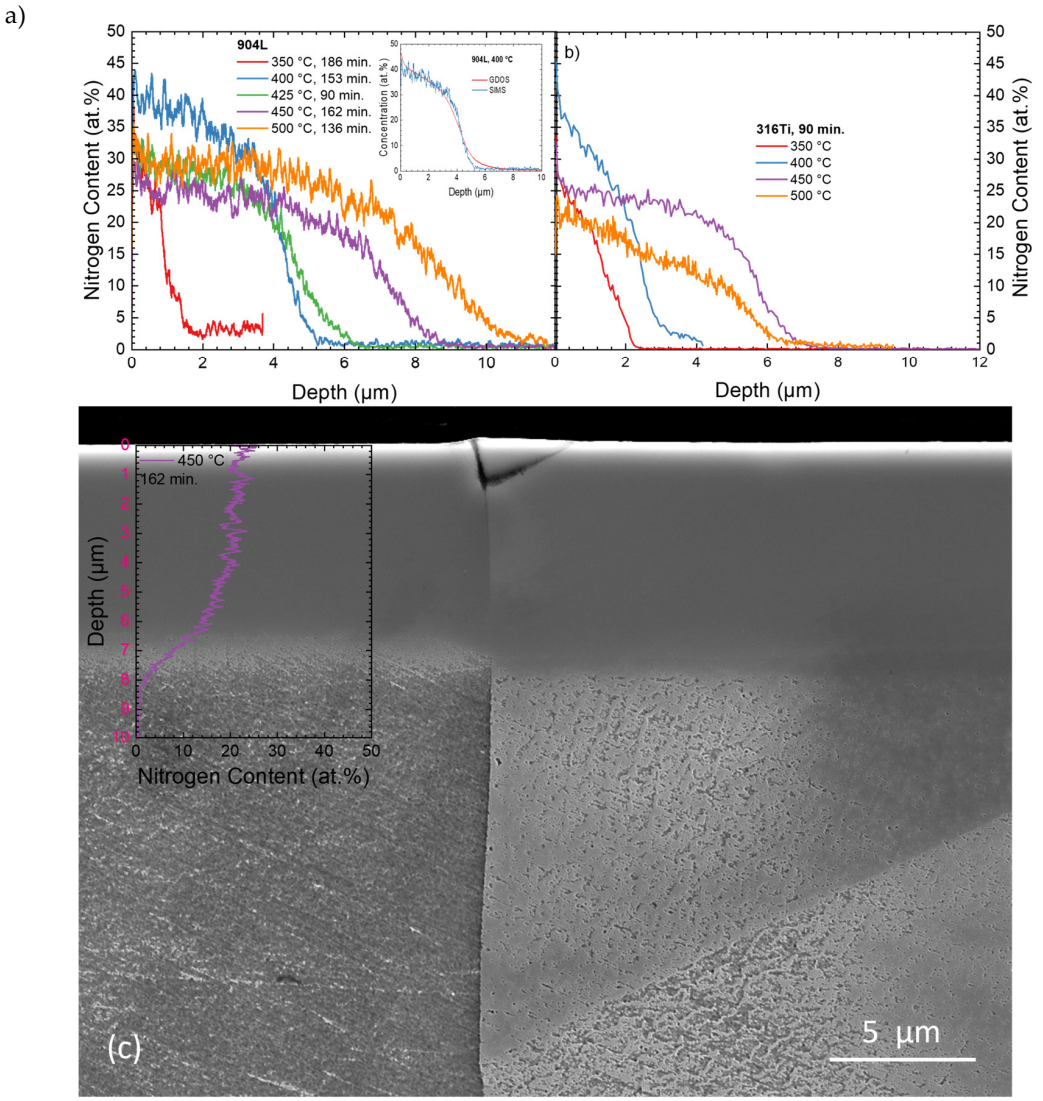


Figure 1. Nitrogen depth profiles after nitriding of steel grade (**a**) 904L and (**b**) 316Ti at different process temperatures and different process times, as obtained from SIMS measurements. In insert, nitrogen depth profile for 904L sample nitrided at 400 °C, measured by SIMS and by GDOES, is shown. (**c**) Micrograph of cross-section for 904L nitrided at 450 °C with the superimposed nitrogen depth profile.

At higher temperatures, a faster diffusion leads to a rather constant surface concentration around 25–30 at.%. The behavior at 350 °C is peculiar. Despite lower diffusivities, less nitrogen is incorporated. Hence, different surface processes—beyond sputtering, especially preferential sputtering (which should be temperature-independent)—must be active. Typically, a temperature-dependent desorption or sticking coefficient is observed in catalytic surface processes, which could also be the underlying effect here.

However, the nitrogen is implanted below the surface, circumventing any absorption and dissociation pathways during nitriding, while the oxide layer is sputtered away within the first minute of the treatment. This should not lead to a delayed nitriding for 904L only at a temperature of 350 °C—even for a hypothetical thicker oxide layer. The reason is that this effect is (again) not temperature-dependent.

Figure 2 depicts the typical time evolution of the XRD diffractograms obtained during nitriding; these are examples of two samples only, both of which were nitrided at 400 °C for different times. As 81 diffractograms were collected during the nitriding time of 160 min, any presentation of all the data in a conventional plot, i.e., “intensity vs. angle” (even with

vertical offsets, cf. the graphical abstract), will lead to a skewed or incomplete presentation. Thus, 2D contour plots were chosen to present the results. Here, the intensity is color-coded (on a logarithmic scale) as a function of time and angle. Thus, the intensity evolution (increase/decrease), as well as the gradual changes in peak positions, is readily identified. However, for a more detailed picture, all the diffractograms must be analyzed in detail.

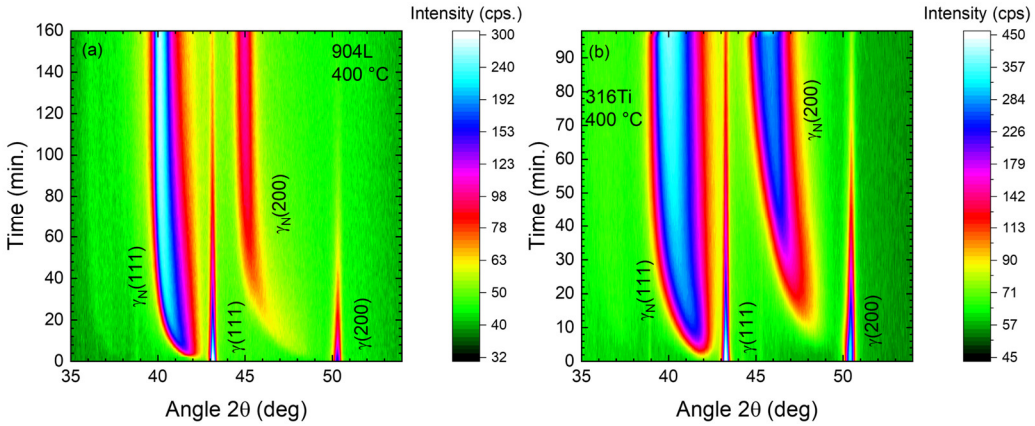


Figure 2. Contour plot of X-ray diffractograms measured during nitriding at 400 °C of stainless steel grade (**a**) 904L and (**b**) 316Ti. Please note the different treatment times of 160 min for 904L and 100 min for 316Ti.

As a starting point, the behavior of both alloys at 400 °C is presented, where no qualitative differences exist between them. For both alloys, a combination of decreasing substrate intensity with the onset of a continuous lattice expansion is observed. Other effects are seen for higher temperatures and are shown below; they include a jump in the lattice expansion at a certain time or the decreasing intensity of the expanded phase after longer times (indicative of the decay and the formation of nanocrystalline, X-ray amorphous CrN precipitates in an FeNi matrix). However, we start now with the growth of the expanded phase as a function of time.

As the expanded phase is always found to have a sharp interface with the substrate in SEM cross-sections, the modelling of the XRD data with a two-layer model (substrate and surface layer) is possible. The artificial broadening of the interface observed in SIMS and GDOES is dominated by the surface roughening of the interface during sputter depth profiling [26] and should be ignored for the analysis. Thus, the (initial) nitrogen diffusivity can be extrapolated from the decreasing substrate intensity (as a function of grain orientation) if the layer thickness is below 5 µm (where the intensity of the scattered X-rays is attenuated to less than 15% compared to the intensity from the surface). The results of the modelling are shown in Figure 3a, which plots the logarithm of the relative intensity vs. the square root of the nitriding time. Assuming an inverse parabolic layer growth, straight lines are expected—and observed, at least for most of the data. Additionally, errors arise from the fitting procedure of the data, especially the uncertainties in the background subtraction.

As with the qualitative results derived from the SIMS depth profiles, a slightly slower diffusion is observed for 350 °C in steel 904L with the intensity calibration using the known attenuation coefficient [22]. Except for this data point, no variation across the steel grade or the grain orientation is observed. This result could be termed fortuitous, as it is known that variations in the grain size even for values larger than the thickness of the nitrided zone can lead to deviations in the diffusion by 50% [27]. The resulting activation energy of 1.0 ± 0.1 eV is identical for both alloys within the error range, thus indicating identical transport pathways within the grains (as is known from the literature [1]). Additionally, the layer thickness from SIMS is converted to a diffusivity, using the known nitriding times. Here, a reasonable agreement between both datasets for the two steel alloys is observed. It must be noted that the SIMS data result in a diffusivity averaged across the

grain orientation, with a slightly higher error due to the inherent roughness increase during sputtering [26].

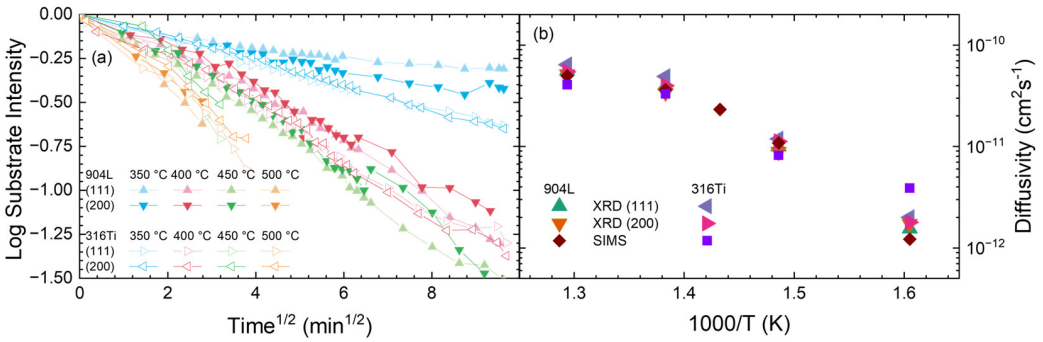


Figure 3. (**a**) Relative intensity of substrate XRD peak in logarithmic scale as a function of square root of process time for 904L and 316Ti steel grade for different process temperatures; (**b**) calculated diffusivity for both type of steels in Arrhenius plot.

Nevertheless, both approaches are complementary: the XRD intensity leads to the initial diffusivity whereas the SIMS measurement calculates an "average" diffusivity across the whole treatment time. As the data are in good agreement, no deviation from the inverse parabolic law can be assumed. The sputtering during nitriding is only a minor corrective term which does not significantly affect the diffusivity of the used short treatments [28]. Conversely, it is difficult or impossible to establish the formation of CrN, which should lead to a different "average diffusivity", as observed in the 5h treatments [29].

3.2. Lattice Expansion

As shown in the previous subsection, the nitrogen content and diffusion are quite similar for both of the investigated alloys. In contrast, the lattice expansion is highly variable between the two alloys, between the process temperatures, and between the grain orientations, as plotted in Figure 4. As a general remark, there is currently no explanation for the evolution of lattice expansion with time; however, existing models of the nitriding of austenitic stainless steel should be able to reproduce this effect [30,31]. With this point in mind, this subsection is more like an empirical data collection where no definitive explanation can yet be provided.

Starting at 350 °C in Figure 4a, despite a similar nitrogen content, a complete reversal of the lattice expansion is seen: 904L, large splitting; 316Ti, small splitting of expansion between orientations; and the (111) expansion is always higher for 316Ti than for 904L during the whole nitriding process.

For longer times, a saturation of the position of all four expanded peaks is apparently obtained. This behavior is mirrored for 400 °C in Figure 4b with a faster saturation (which could be due to a thicker nitrided layer where the interface with the substrate is no longer visible); yet, the (111) expansion is nearly identical for both alloys.

For 450 °C, a different behavior is observed in Figure 4c as the expansion for 316Ti is now lower for both orientations. Still, the (111) expansion saturated quite fast, while the (200) shows a jump for 904L and a gradual increase for 316Ti. This could be due to the formation of a layered structure with two lattice expansions [32], which is investigated in detail below.

For 500 °C in Figure 4d, yet another different behavior is observed: for 904L, the time evolution is very similar to that for 450 °C, whereas for 316Ti a strongly reduced expansion for the (200) oriented grains, even smaller than for the (111) oriented grains at lower temperatures, is measured. At the same time, the formation of CrN precipitates, as indicated by the decreasing intensity of the expanded peak beyond 1 h, is not the cause of this effect. As shown below in Section 3.4, there is still a layered structure, with the CrN-containing layer on top of the expanded austenite and the substrate on the bottom.

At the same time, the Fe-Ni matrix depleted by Cr is converted to a nanoscale ferrite structure [33], which does not contribute to the diffraction intensity at the observed angle of the expanded austenite.

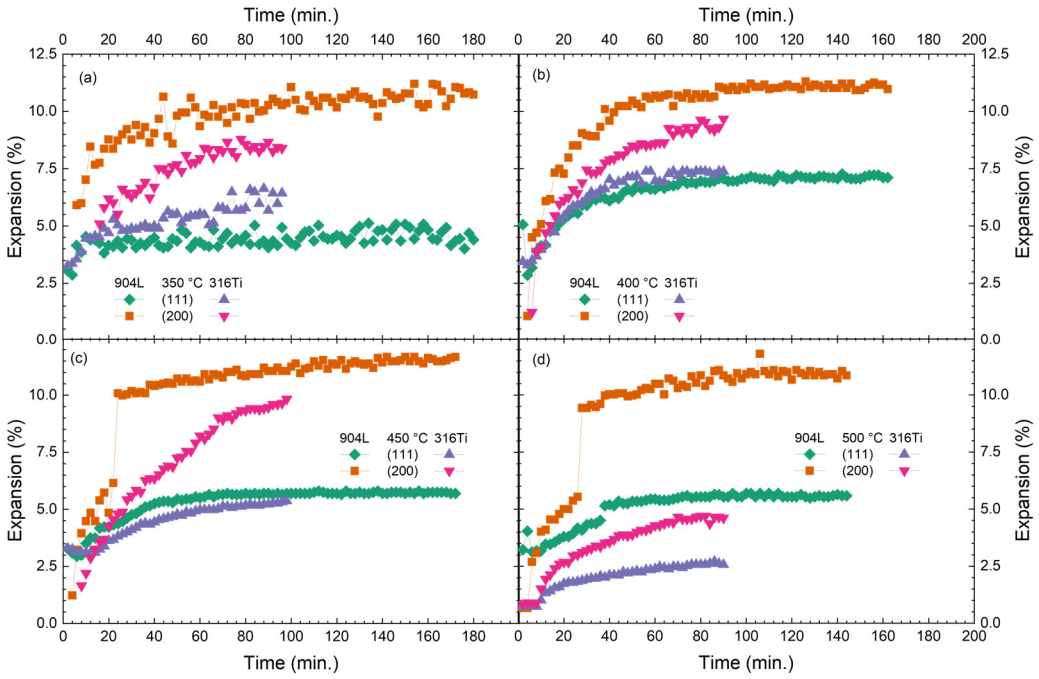


Figure 4. Lattice expansion evolution with increasing time for (111) and (200) orientation for 904L and 316T steel grade for nitriding at (**a**) 350 °C, (**b**) 400 °C, (**c**) 450 °C, and (**d**) 500 °C.

A summary of this behavior is plotted in Figure 5 showing the ratio of the lattice expansion of the (200) oriented vs. the (111) grains as a function of alloy composition, nitriding temperature, and time. The main point here is that there is a huge variation in the ratio of the lattice expansion for the two investigated grain orientations.

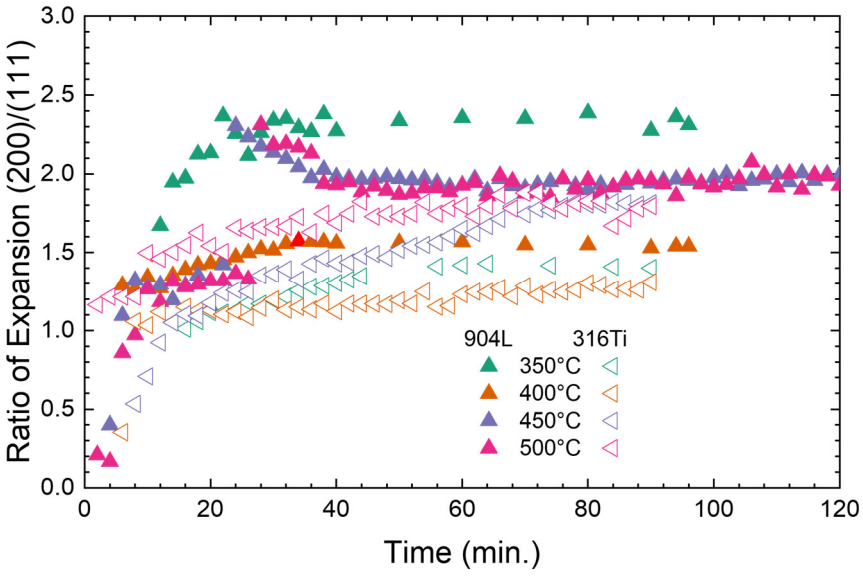


Figure 5. Evolution of ratio of lattice expansion for (111) and (200) orientations with increasing number of diffractograms (respectively, with process time) for 904L and 316Ti steel grades for 4 different process temperatures.

Nevertheless, the first 5–10 min should be treated with caution, as the peak intensity for the expanded peak and the absolute expansion are still small. This introduces an additional error in the fitting routine next to the dominant substrate peak (cf. Figure 2). However, for longer times the plotted values of the lattice expansion are very reliable. In particular, there is only a small concentration gradient of the incorporated nitrogen, and the information depth is heavily skewed towards the surface. The probed depth for the expanded lattice (normal to the surface) is dominated by the first few hundreds of nanometers.

In general, the lattice expansion for the {200} oriented grains is larger than for {111} grains with the absolute values varying between 10 and 150%; larger values are nearly always present for steel 904L compared to 316Ti. Actually, this could be related to the mechanical properties of the underlying steel (or the formed expanded austenite)—and is discussed in more detail in the following paragraphs. However, a big constraint must be inserted: there is a huge variability as a function of processing temperature and processing time—the latter effect would never be visible in ex situ measurements taken after the experiments. For the current in situ experiments, there is nearly no deviation between the last diffractogram measured at the nitriding temperature and the final diffractogram at room temperature. It is negligible beyond the shift due to the thermal expansion; thus, no diffusion or change in the nitrogen distribution occurs during the cooling of the samples.

It was observed before that there are dynamic processes active during nitriding which increase the "scattering intensity" for longer times, especially at intermediate temperatures around 400 °C [23]: the total reflected intensity from the expanded phase is not constant but highly variable. At the same time, the peak width even after correcting for the finite information depth and the nitrogen concentration gradient is also a function of processing temperature [23]. All in all, there are several, mostly unidentified, processes occurring in parallel to the nitrogen insertion and the lattice expansion, including plastic flow due to a stress beyond the yield strength [34], the formation of dislocations [34], or grain rotation [35]. Yet, these phenomena are only the result of underlying processes within the grains and on an atomic level.

Returning to the underlying elastic properties, especially the anisotropy of the elastic modulus in fcc metals, it was proposed that uniaxial stress, together with compositional strain from the isotropic introduction of nitrogen into the lattice [34], can lead to the observed differences in the lattice expansion for differently oriented grains. Yet, there should be a tendency towards a universally valid equation yielding an "anisotropy factor"—similar to the constant which allows the conversion of the lattice parameter into a nitrogen content [34]. Nevertheless, the literature shows that such a simple model, even after correcting for the stacking fault density [36], does not exist. However, variations in the stacking fault energy can affect deformation mechanisms, including dislocation activities and deformation twinning [35].

The only drawback of the in situ method is the limited range in 2θ ending at 54°; thus, only the (111) and (200) oriented grains can be investigated. Here, additional ex situ measurements were performed for the 904L steel samples, and the results are plotted in Figure 6. For the low-orientation reflections—(111) and (200)—no additional information compared to the in situ data is obtained: broad expanded peaks for 350 °C reflect the dominating influence of the gradient within the small layer thickness, compared to the information depth, on the resulting data.

Due to the strong {111} fiber texture, even the higher-order reflections now visible between 60° and 120° in 2θ yield only sparse information. Most of the expanded peaks, broadened for geometrical reasons, are barely visible beyond the noise level. In general, a lattice expansion between 6 and 13% is calculated. This is the same range as already defined by the (111) and (200) reflections and is within the theoretical expectations based on the lattice anisotropy [34]. Thus, even though the ex situ data give additional information on differently oriented grains, no additional insights into the time evolution of the lattice expansion are available.

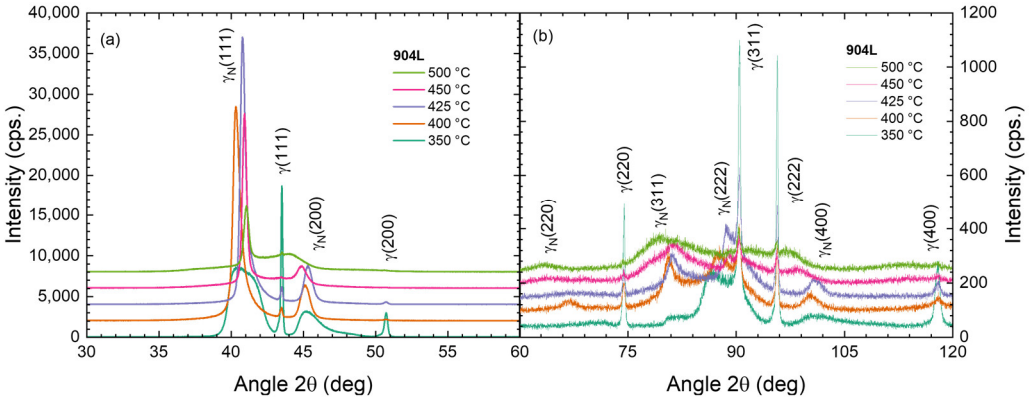


Figure 6. Ex situ measured X-ray diffractograms for 904L steel samples nitrided at different process temperatures, showing the angular range of 2θ from 30° to 120° in two separate panels: (**a**) 30–60° for the (111) reflection and the (200) reflections; (**b**) 60–120° for the region between (220) and (400) reflections.

3.3. Peak Splitting

Another point which is sometimes observed in the literature is peak splitting, which is related to the simultaneous observance of two different expanded peaks, especially for high-alloyed compounds [6]. There, it was argued that a higher Ni content prevents a larger build-up of nitrogen in the surface layers while more Fe is effective in retaining more nitrogen. At the same time, it was proposed that residual stress may induce a sublayer advancement in front of the expanded austenite layer [6].

In previous work, this splitting has been sometimes observed for medium-alloyed steel, e.g., 304 or 316Ti, but only for the (200) oriented grains [30]. There, it was traced to a layered structure with the "low expansion phase" being situated near the interface and the "high expansion phase" near the surface of the sample. While the transition occurred around 1 h after the beginning of the nitriding, at the end of the experiment, after nearly 3 h, only the high-expansion phase was visible in XRD. Subsequent ion etching revealed a surface layer of about 600 nm thickness with the higher expansion (but only in the {200} oriented grain), while no pronounced discontinuity was observed in the nitrogen depth profile [32].

Returning to the current results, both samples implanted here at 450 °C show this (selective) transition in a similar manner, but only for the (200) reflections, as depicted in Figure 7 and evident from Figure 4c. Despite a very similar nitrogen concentration and gradient, the transition occurs earlier in 904L than in 316Ti, and it leads to a thinner layer with a lower lattice expansion. This is evident in the contour plots taken during in situ XRD while sputter-etching the expanded layer, as shown in Figure 7b,d.

Even more pronounced is the effect in Figure 4d for the 904L sample nitrided at 500 °C, where the transition is visible for both orientations. However, there appears to be a slight time delay for the {111} oriented grains. In Figure 4, only the position of the expanded peak with the highest intensity is plotted. When looking at the specific diffractograms, however, the apparent "jump" can be resolved as a function of time (but not depth as the XRD information depth of a few micrometers is still close to the total layer thickness). The layered structure is derived from the sputter investigations shown in Figure 7.

When looking into the details of this transition, as shown in Figure 8, it becomes apparent that the transition is already starting within the first 20 min. There, a new satellite (γ_{N2}) is appearing on the left side of the expanded peak (γ_{N1}) for both orientations and is clearly distinct in the angular position where the intensity is gradually growing. For longer times—near 40 min—this peak is dominating (slightly shifted even further to the left due to the increasing nitrogen content), and the original peak is disappearing.

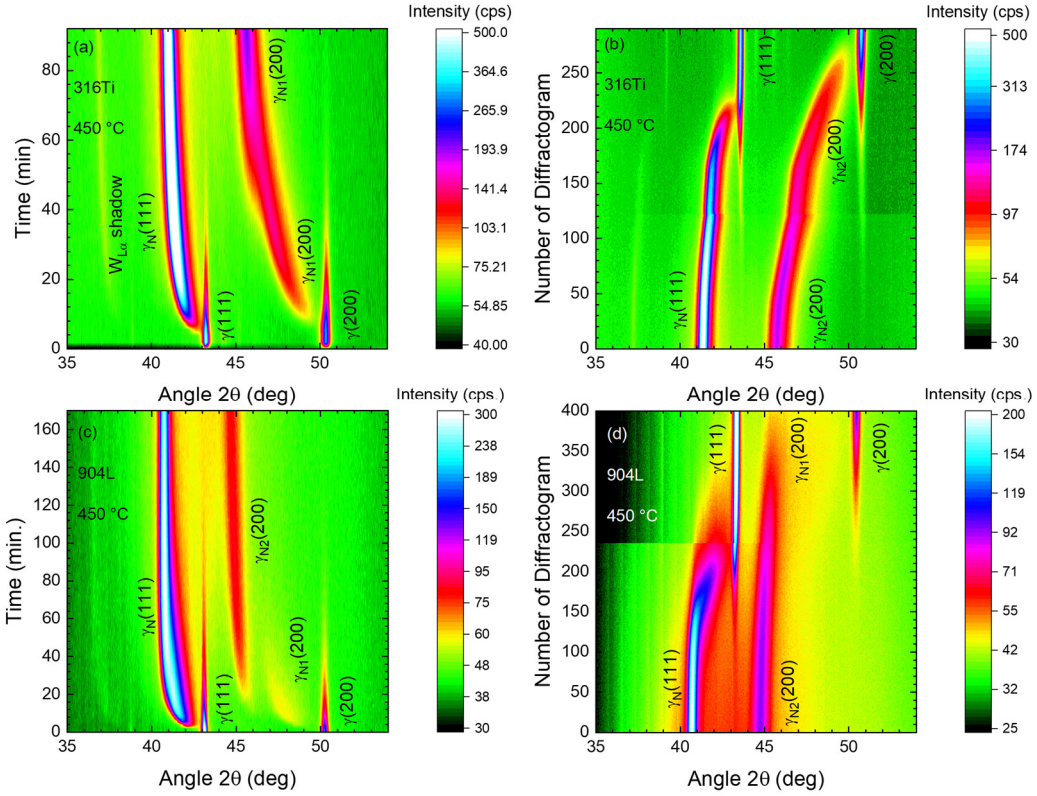


Figure 7. Contour plot of X-ray diffractograms measured during nitriding at 450 °C of (**a**) 316Ti and (**c**) 904L and during sputtering of nitrided samples (**b**) 316Ti and (**d**) 904L. Please note that each ion etching was performed over two days, thus the contour plots show a slight discontinuity. Each diffractogram corresponds to two minutes of sputtering.

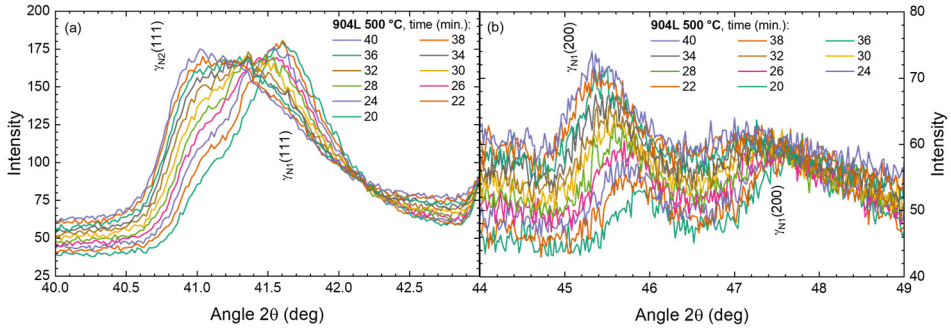


Figure 8. Selected X-ray diffractograms (taken at different times as indicated) measured during nitriding of 904L sample at 500 °C. The diffractograms are vertically shifted for clarity. Please note the different angular scales in both panels: (**a**) (111) reflection and (**b**) (200) reflection.

Thus, it can be concluded that this transition between a low-expansion and a high-expansion phase is observed under some processing conditions during nitriding. As the overlying layer with the high-expansion phase can be quite thick, it often masks the underlying phase in conventional XRD measurement after nitriding. Nevertheless, the transition in the expansion, i.e., the jump ratio, is quite flexible, depending on the temperature, alloy composition, and even the grain orientation. Furthermore, using glancing angle measurements will complicate the analysis as different classes of grains are probed when increasing the angle 2θ [37,38]. At the same time, it has to be kept in mind that only the lattice expansion normal to the surface is probed. Yet, concurrent in-plane measurements yield no unequivocal results about the three-dimensional strain [32].

Hence, a general explanation for the layered expansion is currently not available. One possible candidate is a reduced symmetry, e.g., from fcc to fct symmetry [32,39], with a certain depth or stress necessary to induce the transition. Similarly, work for Ni-based Ni-Ti alloys indicate an origin in the strong depth dependency of the level of residual stress [40].

3.4. Stability of Expanded Austenite

The stability of expanded austenite is crucial for the corrosion resistance as the precipitation of chromium nitride is supposed to prevent the transport of chromium towards the surface [11,24]. Thus, the formation of a protective Cr_2O_3 surface layer is no longer possible at higher temperatures. As the nitrogen is inserted from the surface, the regions closer to the surface experience the nitrogen for a longer time; thus, the CrN formation starts from the surface and progresses towards the bulk [33]. During nitriding, this process is manifested as a decrease in the intensity of the expanded phase after a certain time (cf. Figure 9a beyond 60 min) as the total scattering volume of this phase is decreasing when the CrN precipitates are forming, together with the formation of an Fe-Ni matrix [33]. Initially, the grain size of both phases is too small to be observed by XRD. However, at the end of nitriding, a broad peak at low intensity can be attributed to this nanocrystalline Fe-Ni matrix.

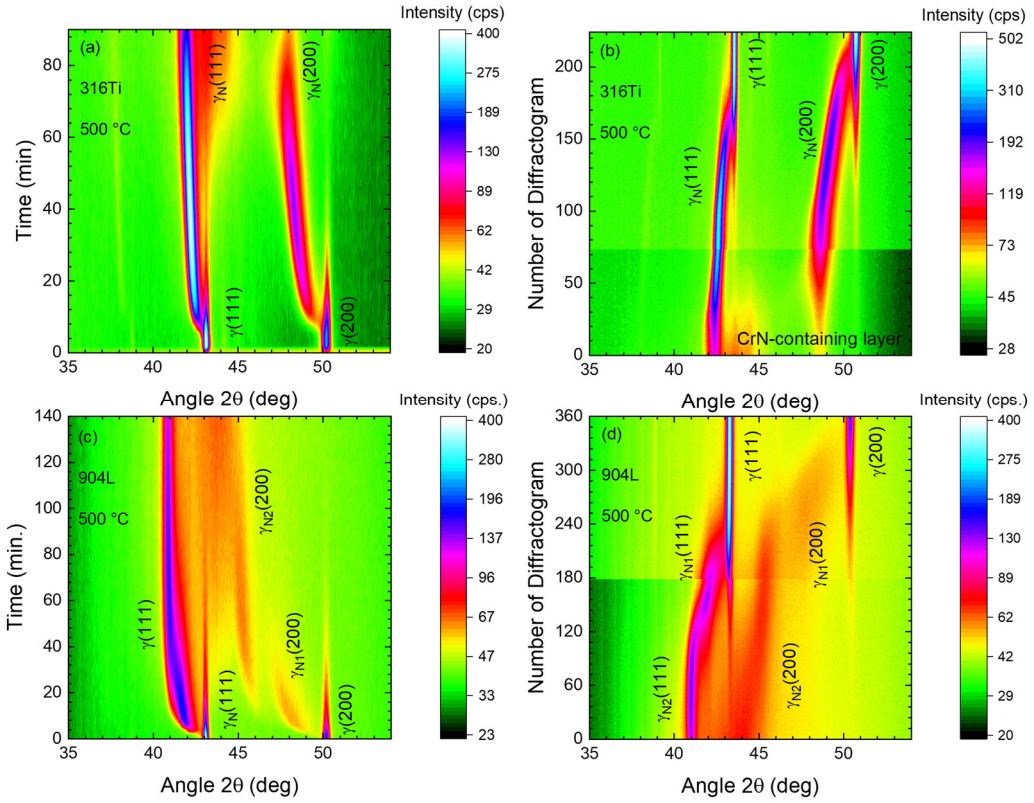


Figure 9. Contour plot of X-ray diffractograms measured during nitriding at 500 °C of steel grade (**a**) 316Ti and (**c**) 904L and during sputtering of nitrided samples of (**b**) 316Ti and (**d**) 904L. Please note that each ion etching was performed over two days; thus, the contour plots show a slight discontinuity. Each diffractogram corresponds to two minutes of sputtering.

As the in situ measurements during nitriding represent the time evolution, integrated over the complete information depth, no actual depth information is obtained there. However, the subsequent sputtering of this layer reveals the structure at the end of nitriding: for 316Ti, a CrN-containing layer on top of expanded austenite followed by the substrate is obtained, whereas for 904L there are two expanded layers on top of each other ($\gamma_{N2}/\gamma_{N1}/\gamma$). This is different from that observed during nitriding as that process is thermally activated—and no depth information is available during nitriding. This layered

structure is shown in Figure 9b for the steel 316Ti, nitrided at 500 °C. In contrast, no such effect is observed for steel 904L nitrided at the same temperature (shown in Figure 9c,d). Thus, it appears that expanded austenite in steel 904L is more stable than in steel 316Ti. However, this would contradict the existing literature where CrN precipitates have been identified in 904L at 500 °C using TEM [17,18].

Here, ToF-SIMS presents an alternative method to probe the atomic environment when looking at the relative intensities of cluster ions. It has been shown that the random arrangement of atoms in steel leads to a certain probability of $FeCr^+$, $FeNi^+$, $CrNi^+$, Fe_2^+, Ni_2^+, and Cr_2^+ molecular cluster ions, with the $Cr_2^+/FeCr^+$ being especially sensitive to the formation of CrN precipitates at the nanoscale [33,41]. Here, atomic rearrangements lead to a preferential ordering [42], where chromium atoms are more likely to be surrounded by nitrogen and other chromium atoms and less likely to be found near iron or nickel atoms.

The corresponding results for the currently investigated samples are shown in Figure 10, exemplifying the contrasting behavior of both alloys: in Figure 10b—for 316Ti—the formation of CrN precipitates is only observed at 500 °C—and then is limited to the first 1.5–2 µm of the nitrided layer. This result confirms the information from the in situ XRD measurements shown in Figure 9b. In contrast, the onset of CrN formation in 904L in Figure 10a is already visible at 450 °C—but not at 425 °C (the intensity ratio of the Cr_2^+ and $FeCr^+$ clusters in SIMS at 425 °C is still identical to that at 350 and 400 °C)—where a (slight) deviation of the $Cr_2^+/FeCr^+$ cluster ion ratio from the straight line, which is characteristic for the lower temperatures, is observed.

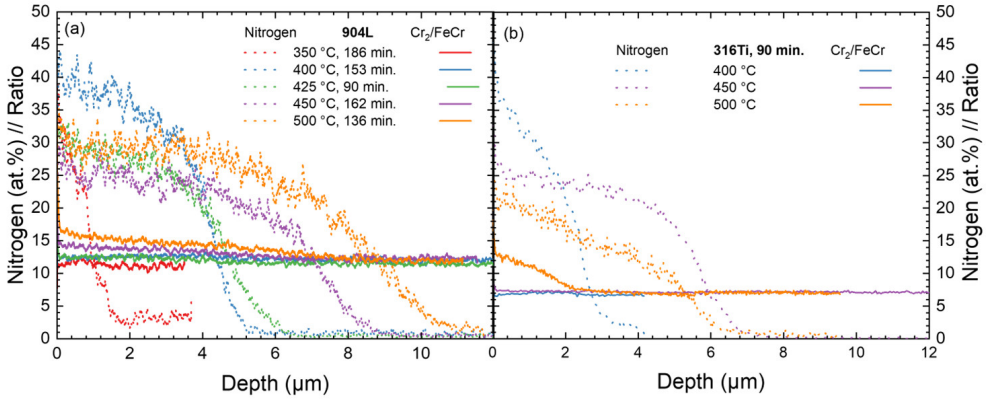


Figure 10. Ratio of intensities for Cr_2 and FeCr cluster ions in ToF-SIMS vs. depth for both steel alloys (steel grade (**a**) 904L and (**b**) 316Ti) at different process temperatures. Additionally, the nitrogen depth profiles after nitriding are shown as dotted lines.

However, the CrN formation is visible in steel 904L across the whole nitrided layer, but at a very low intensity, decreasing from the surface towards the interface. These refined measurements, which are complementary to the in situ XRD data, confirm the observation of CrN precipitates after the nitriding of super austenitic stainless steel in the literature [17,18]. Nevertheless, several open questions remain for further discussion and investigation: why does the nucleation of CrN precipitates start at a much lower temperature in 904L—or at earlier times—during nitriding than in 316Ti? The alloy composition cannot be the only reason as the onset of CrN formation after nitrocarburizing is shifted by about 10 K towards higher temperatures for the higher-alloyed 316L compared to the alloy 304 [29].

At the same time, the growth of these precipitates in 904L is strongly reduced compared to steel 316Ti (or 304 [33]). The scattering intensity of the expanded austenite in steel 904L after nitriding is nearly undisturbed during nitriding as well as ion etching (cf. Figure 9). Thus, the volume fraction of the precipitates, as well as the fraction of a nitrogen- and chromium-free Fe-Ni phase, must be below a few percent of the total volume.

Furthermore, nitriding at 400 °C in an N_2/H_2 atmosphere for extremely long periods, i.e., 99 h, shows that the expanded austenite in 904L is still present, in contrast to 304L,

where CrN is dominant [43]. The higher Ni content is supposed to stabilize the austenite phase and prevent the formation of CrN precipitates. Nevertheless, these are visible, but only in the immediate vicinity of the surface, as shown by the glancing angle measurements at θ = 3° [43]. Prolonged annealing between 450 and 600 °C for 24 to 168 h shows another peculiar behavior as the lattice constant of expanded austenite decreases while no CrN becomes visible (in contrast to 304L, where CrN is visible in XRD) [44]. Localized nitride precipitation (without growth) is assumed to occur.

From an application viewpoint, it would be interesting to investigate the corrosion resistance of super austenitic stainless steel nitrided at higher temperatures (Ref. [18] only compares 300–400 °C) and to establish whether nitriding at even higher temperatures would lead to the growth of CrN precipitates or just a higher nucleation density. At the same time, this could either reduce the processing time or result in a thicker layer, which would be more beneficial for industrial applications.

Here, the nitriding of a Ni-based superalloy (Ni-20Cr) showed a similar effect: an expanded phase with CrN precipitation within this phase while the corrosion resistance was actually slightly improved [45]. Yet, a lattice expansion of 2.3% and 1.0% for the (200) and (111) reflections was measured there, respectively. This was taken as an indication that only a small amount of nitrogen (about 4–10 at.%) was dissolved into the Ni-based superalloy, while the rest of the nitrogen must reside at the grain boundaries or defects. Similarly, a local nitrogen uptake depending on the actual phases present in the material was observed for the nitriding of different Ni-based superalloys with various microstructures [46]. Nevertheless, for the current case of high nitrogen content coupled with a large lattice expansion, the formation of very small CrN precipitates is peculiar and cannot be explained at present.

4. Discussion

For (standard) austenitic stainless steel, no influence of the alloy composition on the nitriding behavior, i.e., nitrogen diffusion, the formation of expanded austenite, and the stability of the expanded phase has been observed [1,4,6]. However, ferritic stainless steel and Ni-based alloys are different in this respect. Ferritic stainless steel shows an expanded phase, sometimes together with an expanded martensite [47]. For austenitic Fe-Ni alloys, in contrast, Fe-rich samples show thicker layers with high N content while Ni-rich samples lead to thinner layers and lower nitrogen content [6].

Looking at the current alloys, 316Ti and 904L, the miniscule addition of Ti (at less than 1 at.%) does not modify the formation of expanded austenite—i.e., nitrogen content and nitrogen diffusion. The formation of TiN instead of CrN has not been observed in TEM investigations [33]. The major difference between the two alloys is the Ni content—12 vs. 25 at.%—and this could be the reason for the difference in the stability of the expanded austenite. According to [6], 904L is still "Fe-rich"; thus, the very similar diffusion and nitrogen content is not surprising; yet, differences in the stacking fault energy do exist [36].

On a microscopic level, dislocation characteristics and their associated strain fields modify the CrN formation [48]. While the insertion of dislocations (due to a stress beyond the yield strength) destroys existing Cr-N chemical pairs, additional nitrogen segregates to the formed dislocations. Thus, segregation of Cr towards nitrogen via the attractive chemical interaction becomes possible. The open question is still whether the different alloy composition, especially the higher Ni content in super austenitic steel, is enough to allow the segregation of isolated Cr-N precipitates, but not the agglomeration of Cr-N clusters.

While the excellent mechanical properties of expanded austenite are well known, and nearly independent of the base material and the nitriding temperature, the corrosion behavior of 904L nitrided at higher temperatures (where CrN clusters, in contrast to CrN precipitates in 316Ti, are formed) is a new topic to be explored in further work.

5. Summary and Conclusions

Using in situ XRD during nitriding as well as ion etching leads to a plethora of information, which is time-resolved but depth-integrated during nitriding, but depth-resolved for the final situation after nitriding at elevated temperatures. While the nitriding of low-alloyed austenitic stainless steel is a common topic, there is nearly no information about super austenitic alloys.

Here, it was shown that the nitrogen uptake and diffusion were very similar for the steels 316Ti and 904L. Between 350 and 500 °C, the diffusion follows an inverse parabolic law with the nitrogen surface concentration between 25 and 40 at.%. No significant difference in the diffusivity was observed when comparing the initial rate, from the decreasing substrate intensity, with the final layer thickness as derived from the SIMS measurements.

In contrast, the lattice expansion (normal to the surface) exhibits a complex behavior depending on temperature, alloy composition, nitriding time, and grain orientation. The main point appears to be that looking at isolated grains is too simplistic; defect formation, grain rotation, and dynamic annealing processes are additionally active and modify the information content of the XRD experiments.

The layered structure with two different lattice expansions (high near the surface and low near the interface—typically around 10% vs. 5%), which is known from the literature, was observed for some conditions, especially at higher nitriding temperatures. For longer times, the surface layer became too thick to see remnants of the interface layer in XRD. A definitive cause could not be identified; strong stress gradients, as proposed in the literature, are a likely candidate.

While not all these results are completely new, the diverging behavior of 316Ti and 904L concerning the formation of CrN precipitates, is unexpected and seen in detail here: 316Ti starts to form CrN precipitates beyond 450 °C, initiated at the surface and progressing towards the interface with a complete decay and the segregation into CrN and an Fe-Ni phase. In contrast, 904L already forms nanoscopic CrN clusters at 450 °C—throughout the whole nitrogen-containing layer, not only at the surface, without subsequent growth or coalescence. At the same time, the original expanded austenite phase is completely undisturbed by this precipitation process. The chemical compositions of the current 904L and the 254 SMO reported in the literature [17,18] are quite similar (X1NiCrMoCu25-20-5 vs. X1CrNiMoCuN20-18-7). Thus, a generalization towards all super austenitic stainless steels is currently not possible, but it could be likely, as the main driving factor of the behavior appears to be the varying Ni content between austenite and super austenite.

The austenitic Fe-Cr-Ni phase is still providing new and unexpected results as soon as the composition deviates from the usual alloys encountered in classical applications of austenitic stainless steel. Unfortunately, we are still relegated to an empirical description of several perplexing effects found during these investigations.

Author Contributions: Conceptualization, D.M.; methodology, D.M.; formal analysis, S.M. and D.M.; writing—original draft preparation, S.M. and D.M.; writing, S.M. and D.M.; funding acquisition, D.M. All authors have read and agreed to the published version of the manuscript.

Funding: This research was funded by Deutsche Forschungsgemeinschaft DFG, grant number MA 4426/5-2.

Data Availability Statement: The raw data supporting the conclusions of this article will be made available by the authors on request.

Acknowledgments: The authors are greatly indebted to H. Neumann and F. Scholze (from IOM) for support during the conception and assembling of the experiment. J.W. Gerlach (from IOM) provided the ex situ XRD measurements. Technical support by M. Müller and R. Woyciechowski (also from IOM) is gratefully acknowledged. The authors thank D. Spemann (from IOM) and J.W. Gerlach for fruitful discussions. M.N. Le, Technische Universität Bergakademie Freiberg, is acknowledged for providing the cross-sectional micrograph.

Conflicts of Interest: The authors declare no conflicts of interest.

References

1. Borgioli, F. From Austenitic Stainless Steel to Expanded Austenite-S Phase. *Metals* **2020**, *10*, 187. [CrossRef]
2. Ichii, K.; Fujimura, K.; Takase, T. Microstructure, corrosion resistance, and hardness of the surface layer in ion nitrided 18-8 stainless steel. *Netsu Shori* **1985**, *25*, 191–195.
3. Somers, M.A.J.; Christiansen, T.L. Low temperature surface hardening of stainless steel. In *Thermochemical Surface Engineering of Steels*; Mittemeijer, E.J., Somers, M.A.J., Eds.; Woodhead Publishing: Oxford, UK, 2015; pp. 557–579.
4. Czerwiec, T.; Renevier, N.; Michel, H. Low-temperature plasma-assisted nitriding. *Surf. Coat. Technol.* **2000**, *131*, 267–277. [CrossRef]
5. Bell, T. Current Status of Supersaturated Surface Engineered S-Phase Materials. *Key Eng. Mater.* **2008**, *373–374*, 289–295. [CrossRef]
6. Williamson, D.L.; Davis, J.A.; Wilbur, P.J. Effect of austenitic stainless steel composition on low-energy, high-flux, nitrogen ion beam processing. *Surf. Coat. Technol.* **1998**, *103–104*, 178–184. [CrossRef]
7. Tao, X.; Matthews, A.; Leyland, A. On the Nitrogen-Induced Lattice Expansion of a Non-stainless Austenitic Steel, Invar 36®, Under Triode Plasma Nitriding. *Metall. Mater. Trans. A* **2020**, *51*, 436–447. [CrossRef]
8. Tang, D.; Zhang, C.; Zhan, H.; Huang, W.; Ding, Z.; Chen, D.; Cui, G. High-Efficient Gas Nitridation of AISI 316L Austenitic Stainless Steel by a Novel Critical Temperature Nitriding Process. *Coatings* **2023**, *13*, 1708. [CrossRef]
9. Luiz, L.A.; Kurelo, B.C.E.S.; de Souza, G.B.; de Andrade, J.; Marino, C.E.B. Effect of nitrogen plasma immersion ion implantation on the corrosion protection mechanisms of different stainless steels. *Mater. Today Commun.* **2021**, *28*, 102655. [CrossRef]
10. Christiansen, T.; Somers, M.A.J. Controlled dissolution of colossal quantities of nitrogen in stainless steel. *Met. Mater. Trans. A* **2006**, *37*, 675–682. [CrossRef]
11. Borgioli, F.; Fossati, A.; Galvanetto, E.; Bacci, T.; Pradelli, G. Glow discharge nitriding of AISI 316L austenitic stainless steel: Influence of treatment pressure. *Surf. Coat. Technol.* **2006**, *200*, 5505–5513. [CrossRef]
12. Drouet, M.; Le Bourhis, E. Low Temperature Nitriding of Metal Alloys for Surface Mechanical Performance. *Materials* **2023**, *16*, 4704. [CrossRef] [PubMed]
13. Czerwiec, T.; Andrieux, A.; Marcos, G.; Michel, H.; Bauer, P. Is "expanded austenite" really a solid solution? Mössbauer observation of an annealed AISI 316L nitrided sample. *J. Alloys Comp.* **2019**, *811*, 151972. [CrossRef]
14. Mittemeijer, E.J.; Somers, M.A.J. Thermodynamics, kinetics, and process control of nitriding. *Surf. Eng.* **1997**, *13*, 483–497. [CrossRef]
15. Borgioli, F. The "Expanded" Phases in the Low-Temperature Treated Stainless Steels: A Review. *Metals* **2022**, *12*, 331. [CrossRef]
16. Totten, G.E.; Casteletti, L.C.; Fernandes, F.A.P.; Gallego, J. Microstructural Characterization of Layers Produced by Plasma Nitriding on Austenitic and Superaustenitic Stainless Steel Grades. *J. ASTM Internat.* **2012**, *9*, 103564. [CrossRef]
17. Fernandes, F.A.P.; Casteletti, L.C.; Gallego, J. Microstructure of nitrided and nitrocarburized layers produced on a superaustenitic stainless steel. *J. Mater. Res. Technol.* **2013**, *2*, 158–164. [CrossRef]
18. Schibicheski Kurelo, B.C.E.; de Souza, G.B.; Serbena, F.C.; Lepienski, C.M.; Chuproski, R.F.; Borges, P.C. Improved saline corrosion and hydrogen embrittlement resistances of superaustenitic stainless steel by PIII nitriding. *J. Mater. Res. Technol.* **2022**, *18*, 1717–1731. [CrossRef]
19. Manova, D.; Bergmann, A.; Mändl, S.; Neumann, H.; Rauschenbach, B. Integration of a broad ion source with a high-temperature vacuum XRD chamber. *Rev. Sci. Instrum.* **2012**, *83*, 113901. [CrossRef] [PubMed]
20. Kaufman, H.R.; Robinson, R.S. Ion Source Design for Industrial Applications. *Am. Inst. Aeronaut. Astronaut. J.* **1982**, *20*, 745–760. [CrossRef]
21. Zeuner, M.; Meichsner, J.; Neumann, H.; Scholze, F.; Bigl, F. Design of ion energy distributions by a broad beam ion source. *J. Appl. Phys.* **1996**, *80*, 611–622. [CrossRef]
22. Henke, B.L.; Gullikson, E.M.; Davis, J.C. X-ray Interactions: Photoabsorption, Scattering, Transmission, and Reflection at E = 50–30,000 eV, Z = 1–92. *At. Data Nucl. Data Tables* **1993**, *54*, 181–342. [CrossRef]
23. Manova, D.; Schlenz, P.; Mändl, S. A combination of ion beam sputtering and in-situ X-ray diffraction as a method for depth resolved phase analysis using nitrogen implanted austenitic stainless steel as an example. *J. Appl. Phys.* **2022**, *131*, 025306. [CrossRef]
24. Williamson, D.L.; Ozturk, O.; Wei, R.; Wilbur, P.J. Metastable phase formation and enhanced diffusion in f.c.c. alloys under high dose, high flux nitrogen implantation at high and low ion energies. *Surf. Coat. Technol.* **1994**, *65*, 15–23. [CrossRef]
25. *DIN EN ISO 17025*; Allgemeine Anforderungen an die Kompetenz von Prüf- und Kalibrierlaboratorien. DIN Media GmbH: Berlin, Germany, 2018. [CrossRef]
26. Manova, D.; Díaz, C.; Pichon, L.; Abrasonis, G.; Mändl, S. Comparability and Accuracy of Nitrogen Depth Profiling in Nitrided Austenitic Stainless Steel. *Nucl. Instrum. Meth. B* **2015**, *349*, 106–113. [CrossRef]
27. Manova, D.; Mändl, S.; Neumann, H.; Rauschenbach, B. Influence of Grain Size on Nitrogen Diffusivity in Austenitic Stainless Steel. *Surf. Coat. Technol.* **2007**, *201*, 6686–6689. [CrossRef]
28. Mändl, S. Nitriding of Stainless Steel: PIII or Low Energy Nitriding? *Plasma Proc. Polym.* **2007**, *4*, 239–245. [CrossRef]
29. Jafarpour, S.M.; Martin, S.; Schimpf, C.; Dalke, A.; Biermann, H.; Leineweber, A. Comparative Plasma Nitrocarburizing of AISI 316L and AISI 304 Steels Using a Solid Carbon Active Screen: Differences in the Developing Microstructures. *Metall. Mater. Trans. A* **2024**, *55*, 1588–1599. [CrossRef]

30. Christiansen, T.; Dahl, K.V.; Somers, M.A.J. Nitrogen diffusion and nitrogen depth profiles in expanded austenite: Experimental assessment, numerical simulation and role of stress. *Mater. Sci. Technol.* **2008**, *24*, 159–167. [CrossRef]
31. Pranevicius, L.; Templier, C.; Rivière, J.-P.; Méheust, P.; Pranevicius, L.L.; Abrasonis, G. On the mechanism of ion nitriding of an austenitic stainless steel. *Surf. Coat. Technol.* **2001**, *135*, 250–257. [CrossRef]
32. Manova, D.; Schlenz, P.; Gerlach, J.W.; Mändl, S. Depth-Resolved Phase Analysis of Expanded Austenite formed in Austenitic Stainless Steel. *Coatings* **2020**, *10*, 1250. [CrossRef]
33. Manova, D.; Lotnyk, A.; Mändl, S.; Neumann, H.; Rauschenbach, B. CrN Precipitation and Elemental Segregation during the Decay of Expanded Austenite. *Mater. Res. Express* **2016**, *3*, 066502. [CrossRef]
34. Czerwiec, T.; He, H.; Marcos, G.; Thiriet, T.; Weber, S.; Michel, H. Fundamental and Innovations in Plasma Assisted Diffusion of Nitrogen and Carbon in Austenitic Stainless Steels and Related Alloys. *Plasma Proc. Polym.* **2009**, *6*, 401–409. [CrossRef]
35. Templier, C.; Stinville, J.C.; Villechaise, P.; Renault, P.O.; Abrasonis, G.; Rivière, J.P.; Martinavičius, A.; Drouet, M. On lattice plane rotation and crystallographic structure of the expanded austenite in plasma nitrided AISI 316L steel. *Surf. Coat. Technol.* **2010**, *204*, 2551–2558. [CrossRef]
36. Wagner, C.; Laplanche, G. Effects of stacking fault energy and temperature on grain boundary strengthening, intrinsic lattice strength and deformation mechanisms in CrMnFeCoNi high-entropy alloys with different Cr/Ni ratios. *Acta Mater.* **2023**, *244*, 118541. [CrossRef]
37. Lutz, J.; Manova, D.; Gerlach, J.W.; Störmer, M.; Mändl, S. Interpretation of Glancing Angle and Bragg-Brentano XRD Measurements for CoCr Alloy and Austenitic Stainless Steel after PIII Nitriding. *IEEE Trans. Plasma Sci.* **2011**, *39*, 3056–3060. [CrossRef]
38. Feugeas, J.; Gómez, B.; Craievich, A. Ion nitriding of stainless steels. Real time surface characterization by synchrotron X-ray diffraction. *Surf. Coat. Technol.* **2002**, *154*, 167–175. [CrossRef]
39. Fewell, M.P.; Mitchell, D.R.G.; Priest, J.M.; Short, K.T.; Collins, G.A. The nature of expanded austenite. *Surf. Coat. Technol.* **2000**, *131*, 300–306. [CrossRef]
40. Fonovic, M.; Leineweber, A.; Robach, O.; Jägle, E.A.; Mittemeijer, E.J. The Nature and Origin of "Double Expanded Austenite" in Ni-Based Ni-Ti Alloys Developing Upon Low Temperature Gaseous Nitriding. *Met. Mater. Trans. A* **2015**, *46*, 4863–4874. [CrossRef]
41. Manova, D.; Gerlach, J.W.; Mändl, S. Nitrogen isotope marker experiments in austenitic stainless steel for identification of trapping/detrapping processes at different temperatures. *Surf. Coat. Technol.* **2023**, *472*, 129952. [CrossRef]
42. Che, H.L.; Yang, X.; Lei, M.K.; Somers, M.A.J. Co-existence of γ'N phase and γN phase on nitrided austenitic Fe-Cr-Ni alloys—III. An investigation of the evolution of long-range ordered domains. *Acta Mater.* **2023**, *253*, 118971. [CrossRef]
43. Cao, Y.; Maistro, G.; Norell, M.; Pérez-García, S.A.; Nyborg, L. Multi-technique characterization of low-temperature plasma nitrided austenitic AISI 304L and AISI 904L stainless steel. *Surf. Interface Anal.* **2014**, *46*, 856–860. [CrossRef]
44. Maistro, G.; Pérez-García, S.A.; Norell, M.; Nyborg, L.; Cao, Y. Thermal decomposition of N-expanded austenite in 304L and 904L steels. *Surf. Eng.* **2016**, *33*, 319–326. [CrossRef]
45. Xu, X.L.; Yu, Z.W.; Cui, L.Y. Microstructure and properties of plasma nitrided layers on Ni-based superalloy Ni-20Cr. *Mater. Charact.* **2019**, *155*, 109798. [CrossRef]
46. Chollet, S.; Pichon, L.; Cormier, J.; Dubois, J.B.; Villechaise, P.; Drouet, M.; Declemy, A.; Templier, C. Plasma assisted nitriding of Ni-based superalloys with various microstructures. *Surf. Coat. Technol.* **2013**, *235*, 318–325. [CrossRef]
47. Borgioli, F. Formation of expanded phases in ferritic stainless steel nitrided at low temperatures. *Surf. Coat. Technol.* **2024**, *477*, 130309. [CrossRef]
48. Kawahara, Y.; Kobatake, S.; Kaneko, K.; Sasaki, T.; Ohkubo, T.; Takushima, C.; Hamada, J. Combined effect of interstitial-substitutional elements on dislocation dynamics in nitrogen-added austenitic stainless steels. *Sci. Rep.* **2024**, *14*, 4360. [CrossRef]

Disclaimer/Publisher's Note: The statements, opinions and data contained in all publications are solely those of the individual author(s) and contributor(s) and not of MDPI and/or the editor(s). MDPI and/or the editor(s) disclaim responsibility for any injury to people or property resulting from any ideas, methods, instructions or products referred to in the content.